
Varying Manifolds in Diffusion: From Time-varying Geometries to Visual Saliency

Junhao Chen
Shandong University
jhochen@mail.sdu.edu.cn

Manyi Li*
Shandong University
manyili@sdu.edu.cn

Zherong Pan
Tencent America
zherong.pan.usa@gmail.com

Xifeng Gao
Tencent America
gxf.xisha@gmail.com

Changhe Tu
Shandong University
chtu@sdu.edu.cn

Abstract

Deep generative models learn the data distribution, which is concentrated on a low-dimensional manifold. The geometric analysis of distribution transformation provides a better understanding of data structure and enables a variety of applications. In this paper, we study the geometric properties of the diffusion model, whose forward diffusion process and reverse generation process construct a series of distributions on manifolds which vary over time. Our key contribution is the introduction of generation rate, which corresponds to the local deformation of manifold over time around an image component. We show that the generation rate is highly correlated with intuitive visual properties, such as visual saliency, of the image component. Further, we propose an efficient and differentiable scheme to estimate the generation rate for a given image component over time, giving rise to a generation curve. The differentiable nature of our scheme allows us to control the shape of the generation curve via optimization. Using different loss functions, our generation curve matching algorithm provides a unified framework for a range of image manipulation tasks, including semantic transfer, object removal, saliency manipulation, image blending, etc. We conduct comprehensive analytical evaluations to support our findings and evaluate our framework on various manipulation tasks. The results show that our method consistently leads to better manipulation results, compared to recent baselines.

1 Introduction

Modern deep learning architectures rely on a fundamental principle: high-dimensional data resides on a low-dimensional manifold. This principle of dimensionality reduction underlies many recent advancements in generative models, such as Variational Autoencoders (VAEs) [1] and Generative Adversarial Networks (GANs) [2], which capture the essential structure of data by learning efficient, low-dimensional representations. Building on these low-dimensional embeddings, a representative approach to learning data distributions involves constructing transformations between the data distribution and a Gaussian distribution. This method allows for the representation of any probability distribution while introducing a geometric mapping that enables further understanding of data structure. For instance, the analysis of the geometric properties of both the data and latent manifolds in GANs enables applications like geodesic interpolation [3, 4].

*Corresponding author.

Most recently, diffusion models [5, 6] have significantly improved the expressivity of generative models, more effectively enabling a single model to represent diverse internet images in the wild. Since then, the analysis of data distributions learned by diffusion models has garnered much attention from researchers. However, this analysis is more challenging than for prior models due to the transformation between the data distribution and Gaussian distribution involving the entire forward diffusion process, leading to time-varying geometric mappings.

In this paper, we propose a metric to gauge the rate of change in the manifold as a function of time. As our key observation, we show that such a change rate corresponds to the rate of information removal during the diffusion process, or the rate of information injection during the reverse generation process. Therefore, we call our metric in the reverse process the "*generation rate*", which changes over time to define the "*generation curve*". Further, we propose an efficient and differentiable scheme to approximate the generation rate in the observation space (image space for 2D diffusion models). Utilizing its differentiable nature, we can then manipulate the shape of the generation curve by stochastic optimization, i.e., to match the shape of the curve with a given reference curve. Finally, we show that such optimization corresponds to a unified framework for a range of image manipulation tasks, such as semantic transfer, object removal, saliency manipulation, and image blending. By comprehensively evaluating our approach in all these tasks, we confirm that our framework consistently outperform existing state-of-the-art models.

2 Background

2.1 Diffusion Process as Stochastic Differential Equations

The diffusion model [5, 6] is a type of stochastic generative model that gradually adds noise to the original data in a forward diffusion process and generates realistic data samples via a reverse denoising process. It can be formulated as stochastic differential equations (SDEs) [7] with a continuous time variable $t \in [0, T]$. The forward diffusion process, which evolves a probabilistic distribution towards a more uniform or stable state over time through random perturbations, is written as:

$$dX_t = \mu(X_t, t) dt + \sigma(X_t, t) dW_t, \quad (1)$$

where X_t represents the state of the process at time t , $\mu(X_t, t)$ is the drift coefficient, $\sigma(X_t, t)$ is the volatility coefficient, and dW_t is the differential of a Wiener process.

The reverse SDE, used for denoising and generating data, is formulated as:

$$dX_t = [\mu(X_t, t) - \sigma^2(X_t, t) \nabla_x \log p_t(X_t)] dt + \sigma(X_t, t) dW_t, \quad (2)$$

where $\nabla_x \log p_t(X_t)$ is the score function of the probability density function $p_t(X_t)$.

We can further derive a deterministic process with trajectories that share the same marginal probability densities as the SDE (Eq. 1). This is formulated as an ordinary differential equation (ODE) [7]:

$$dX_t = [\mu(X_t, t) - \frac{1}{2} \sigma^2(X_t, t) \nabla_x \log p_t(X_t)] dt, \quad (3)$$

In this paper, we adopt this deterministic approach and use its specific discrete form from [8]:

$$\frac{X_{t-\Delta t}}{\sqrt{\alpha_{t-\Delta t}}} = \frac{X_t}{\sqrt{\alpha_t}} + \left(\sqrt{\frac{1-\alpha_{t-\Delta t}}{\alpha_{t-\Delta t}}} - \sqrt{\frac{1-\alpha_t}{\alpha_t}} \right) \epsilon_\theta^t(X_t), \quad (4)$$

where α_t is a time-dependent variable as defined in [8] and $\epsilon_\theta^t(X_t)$ is a neural network with parameter θ trained to approximate the score function $\nabla_x \log p_t(X_t)$. In this form, one can directly obtain a predicted \hat{X}_0 from the linear approximation of X_t by: $\hat{X}_0(X_t) = (X_t - \sqrt{1-\alpha_t} \epsilon_\theta^t(X_t)) / \sqrt{\alpha_t}$, which can further be used as an estimation of the generation state.

2.2 Geometric Analysis of Data Manifold

It is widely accepted that the distribution of high-dimensional observed data, i.e. the distribution of open-domain images, resides on a low-dimensional manifold M embedded in the high-dimensional Euclidean space R^d [9, 10]. From this perspective, generative models such as VAE [1] and GAN [2]

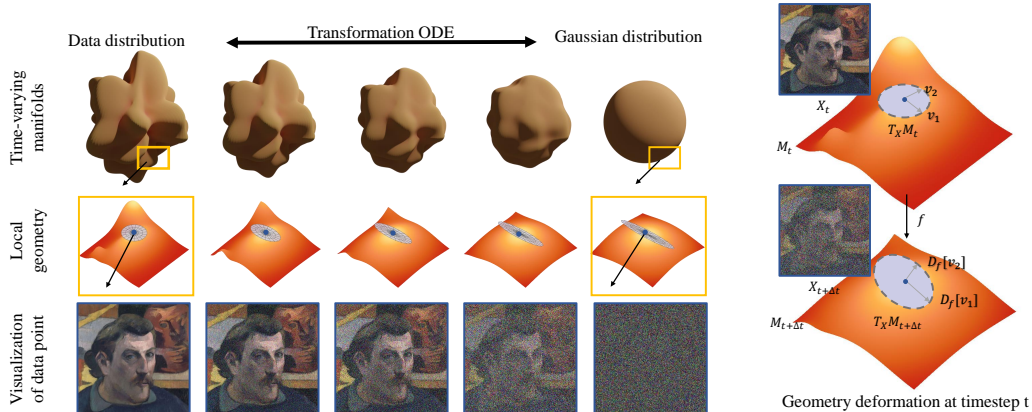


Figure 1: The time-varying manifolds in diffusion process and the local geometric transition.

learn the mapping from a simple latent space Z , usually a Gaussian distribution, to the data manifold M . Geometric analysis of these manifold mappings [3, 4] provides a valuable tool for studying the structures of both data and latent manifolds, enabling various applications [3, 4, 11, 3].

The tangent space $T_x M$ computed on manifolds is crucial for local analysis [12, 13, 14]. It has been shown that using local contraction as a penalty during the training of auto-encoders results in better latent representations that are locally invariant to perturbations in the noise directions of the raw input [12], through which the tangent space is approximately spanned by the subset of singular vectors corresponding to largest singular values from encoding mapping (see e.g. [15]). Moreover, in GANs, the open set formed by latent variables ensures that the Jacobian of the generator directly spans the tangent space [14, 4]. Analyzing directional contraction in such mappings enables the unsupervised discovery of semantically disentangled image editing directions [16, 17].

The generative process of diffusion models can be seen as iteratively modifying a manifold to approximate the true data manifold. This process can be modeled as a series of manifolds denoted as $\{M_t\}$, as shown in Figure 1. Regrettably, for diffusion transformations built on the Euclidean observation space, unlike the straightforward mappings available in VAEs and GANs, the manifolds $\{M_t\}$ lack a direct mapping to a compact latent space. This absence complicates the geometric analysis of the manifold M_t . Fortunately, for diffusion models with a U-Net architecture, prior works [18, 19] have empirically discovered that the encoder layers of the score predictor U-Net can be interpreted as a mapping, denoted as h_t , from the transient manifold to a (transient) compact latent space \hat{H}_t . In practice, we can use the power method [20, 19] to approximate the leading right singular vectors of the Jacobian matrix J_{h_t} of h_t that span the tangent space $T_x M_t$.

3 Generation Rate & Generation Curve

In this section, we first define our notation of generation rates and generation curves (Section 3.1), and then propose an efficient scheme to approximately compute these curves (Section 3.2). Finally, we show that these curves correspond to the rate at which the diffusion model generates visual contents, and the fluctuation exhibits high correlation with the visual saliency (Section 3.3).

3.1 Definition

The key idea in our analysis lies in the temporally local analysis of the time-varying manifolds $\{M_t\}$. Between these consecutive manifolds, we define the mapping corresponding to the forward diffusion process as $X_t = f_t(X_{t-\Delta t})$, and the mapping corresponding to the reverse diffusion process as $X_{t-\Delta t} = f_t^{-1}(X_t)$. Instead of analyzing the mapping f from the latent space to the data manifold, as has been done for GANs and VAEs, we analyze the local geometric distortion between two temporally consecutive manifolds. Following a similar reasoning as prior works [12, 15], we represent the distortion through the deformation between tangent spaces, which can be derived from the Jacobian matrix J_f of the mapping f . Specifically, the scaling of a tangent vector is represented

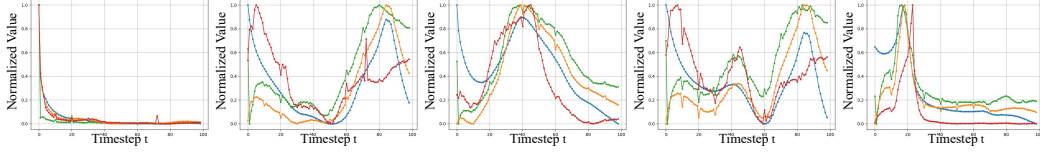


Figure 2: The generation curves approximated by four different methods: $\|D_{f^{-1}}(X_t)[\text{Proj}(v)]\|$ •, $\|\nabla_x^2 \log p_t(X_t) \cdot \text{Proj}(v)\|$ •, $\|D_{h_t}(X_t)[\text{Proj}(v)]\|$ •, $\|D_{h_t}(X_t)[v]\|$ •, normalized into range $[0, 1]$.

by its corresponding singular value. An important empirical finding is that, under the parametrization in Eq. 4, the singular values of J_f for tangent vectors almost always fall in the range $(0, 1)$, implying that f_t is a contracting mapping when restricted to M_t . This is consistent with the fact that the diffusion process removes information from the data and injects entropy into the distribution on M_t as t increases. Similarly, we can consider the reverse process and the associated map f_t^{-1} , whose Jacobian $J_{f^{-1}}$ empirically has singular values in the range $(1, \infty)$. This corresponds to the process of injecting information into the distribution by reducing its entropy. Using these observations, we define our information generation rate as the norm of the directional derivative:

$$D_{f^{-1}}(X_t)[v] : T_x M_t \mapsto T_x M_{t-\Delta t}, \quad (5)$$

along a tangent-space variation v in the observation space. Intuitively, for two images noised to the level t and separated by v in the observation space, they are separated by $\|D_{f^{-1}}(X_t)[v]\|$ in the previous noised level $t - \Delta t$. The variation vector v provides us with an important extra degree of freedom, allowing us to investigate the generation rate in a subset of the observation space. For example, by setting v to correspond to a specific image component, we can observe the generation rate for that component. The selection of v is crucial to our various image manipulation tasks.

A potential pitfall of Eq. 5 lies in the requirement that v is a tangent-space variation. In practice, however, an arbitrarily sampled variation $v \in R^d$ to a noised image X_t might not lie in the tangent space $T_x M_t$. To mitigate this flaw, we define the projection operator $\text{Proj}(v)$ as the projection of v into the subspace of the first K leading singular vectors. Combining these definitions, we define the projected generation rate:

$$r_t(X_t, v) \triangleq \|D_{f^{-1}}(X_t)[\text{Proj}(v)]\|, \quad (6)$$

which allows an arbitrary variation v in the ambient space to be used. We then define the generation curve $c(X_T, v)$ as the curve of $r_t(X_t, v)$ calculated over all discrete time instances during the entire generation process for a fixed variation v , starting from X_T for $t \in [0, T]$. Assuming the fixed path $\{X_0, X_1, \dots, X_T\}$ derived from Eq. 4, any variable X_t corresponds to the same curve. Therefore, we do not distinguish between the input variables, i.e. $c(X_T, v) \triangleq c(X_0, v)$.

3.2 Approximate Computation of Generation Curve

Regretfully, it is challenging to further apply $c(X_T, v)$ in applications as the projection operation $\text{Proj}(v)$ requires the calculation of the tangent space at each moment. In the context of using the leading singular vectors of J_h as the tangent basis, the need for Singular Value Decomposition (SVD) often makes it non-differentiable, especially when applying power methods for high-dimensional data. In this section, we propose a practical approximation scheme for the computation of the generation rate $r_t(X_t, v)$. We start by rewriting the generation rate based on Eq. 4:

$$D_{f^{-1}}(X_t) = A(t)I + B(t)\nabla_x^2 \log p_t(X_t), \quad (7)$$

where $A(t)$ and $B(t)$ are time-dependent terms, I is the identity matrix, and $\nabla_x^2 \log p_t(X_t)$ is the Hessian of $\log p_t(X_t)$. We note that the content of the noised image is contained in the score function, so we discard other terms and approximate:

$$\|D_{f^{-1}}(X_t)[\text{Proj}(v)]\| \approx \|\nabla_x^2 \log p_t(X_t) \cdot \text{Proj}(v)\|. \quad (8)$$

Next, we utilize the fact that the output space of mapping h_t is the bottleneck for the score-function predicting network $\epsilon_\theta^t(X_t)$. Thus, we propose replacing the differential of $\epsilon_\theta^t(X_t)$ with that of h :

$$\|\nabla_x^2 \log p_t(X_t) \cdot \text{Proj}(v)\| \approx \|D_{h_t}(X_t)[\text{Proj}(v)]\|. \quad (9)$$

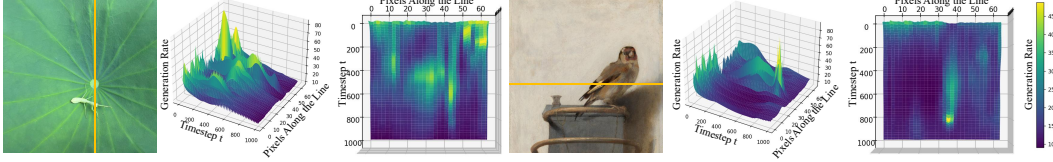


Figure 3: Generation curves for a column or row of image pixels (yellow). The generation curves fluctuate significantly at the pixels with high visual saliency, such as the wing tip of the bird.

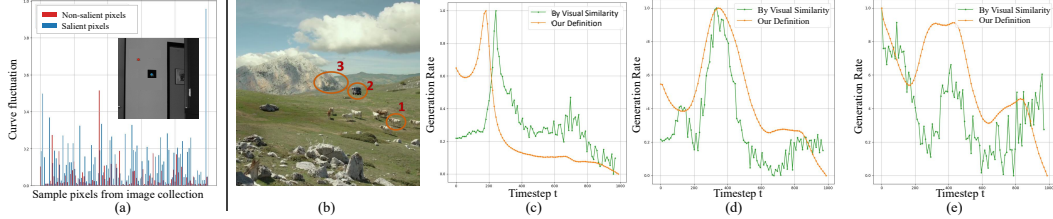


Figure 4: Left: visual saliency analysis with (a) curve fluctuation statistics of salient (blue) and non-salient (red) pixels as well as an example image. Right: generation curves at spatial locations on the image (b). (c), (d) and (e) show the perceptual-based (green) and our generation curve (orange) corresponding to the specified three regions.

Given that H_t itself is a compact latent space, as introduced in Section 2, the forward differential $D_{h_t}(X_t)[v]$ of any vector v closely approximates the tangent space estimated by h_t . Therefore, we omit the projection operator and approximate the generation rate by:

$$\begin{aligned} r_t(X_t, v) &= \|D_{f_t^{-1}}(X_t)[\text{Proj}(v)]\| \approx \|\nabla_x^2 \log p_t(X_t) \cdot \text{Proj}(v)\| \\ &\approx \|D_{h_t}(X_t)[\text{Proj}(v)]\| \approx \|D_{h_t}(X_t)[v]\|. \end{aligned} \quad (10)$$

In Figure 2, we plot the generation curve with $r_t(X_t, v)$ approximated by four different methods. As expected, the four curves exhibit a similar trend, with critical points appearing at comparable noise levels (diffusion time). Although the exact values of these curves differ due to variations in space, their trend is sufficient for further analysis and image manipulation tasks. Since the evaluation of the last approximation $\|D_{h_t}(X_t)[v]\|$ is the most computationally efficient and inherently differentiable, we adopt this approximation scheme in our subsequent analysis and applications.

3.3 Connection to Visual Saliency

In this section, we present our comprehensive analysis showing that the generation curve is strongly connected to visual properties on images. To this end, we set the vector v as a unit vector $v = e_{ij}$ that takes the value 1 at ij -th pixel and zero otherwise. This setting allows us to investigate the rate of information generation for a single channel of a pixel. Considering the additive generation rate, we define the generation rate of a pixel as the average of its internal channels. In implementation, we take the 0-th channel to represent a pixel for the acceleration purpose, due to the characteristics of latent diffusion model (LDM) [21] as described in Appendix B.

In Figure 3, we plot the generation curve for a column or row of image pixels. We noticed that pixels with high visual saliency, such as the wing tip and the body of the bird, the generation curve fluctuates significantly. At other locations, the curve becomes much smoother except for a sharp rise when t approaches 0. We further conduct a large-scale analysis by using 100 pictures from the visual saliency dataset [22]. For each image, we sample one salient pixel and one non-salient pixel from the ground truth. For both pixels, we take the windowed variance to measure the fluctuation of its generation curve, and the statistics are shown in figure 4. (Refer to Appendix B.1 for more details.) For 86% of the images, higher visual saliency leads to higher fluctuation, validating the consistent correspondence between curve fluctuation and visual saliency.

For other morphological factors of the curve beyond its fluctuation, such as the position and curvature of the peaks, we experimentally found that these are determined by more specific and low-level visual

properties of the object. For instance, image patches with different materials like grass and ground exhibit different curve shapes even though they share similar visual saliency.

We further notice an alternative way of defining the generation rate, which is inspired by the generation state derived from [8]. For each noised image X_t , we can compare the visual similarity of its predicted \hat{X}_0 to the real image X_0 , e.g., by computing the perceptual distance [23, 24] between the two images. Such computation can be performed with respect to an image patch by applying a region mask. We consider this similarity as the generation state, and the time derivative of this state can also be interpreted as the generation rate. In Figure 4, we compare the generation curve computed using our definition and this alternative definition for objects (details in Appendix B.2). We notice that the two curves exhibit similar trends while our curve has much less noise. Besides, due to the nature of visual metrics, this method is applicable only to regions with semantically complete objects, and often exhibits heavy noise or even negative generation rates in areas with less prominent visual features, especially with background patches. These limitations prevent this alternative method from providing reliable indications of the information generation rate, limiting its usage in assisting other tasks, such as observing the generation process of objects, or selecting an editing timestep [18, 25].

4 Curve Matching

We utilize the differentiable scheme of our generation rate to define an optimization procedure applicable to various image manipulation tasks. Since the generation curve is intrinsically related to certain visual properties, it enables us to manipulate those properties by modifying the curves. For simplicity, we take single-channel images to describe our algorithm. In practice, we enumerate all the channels of the images and invoke our algorithm equivalently.

The proposed curve matching algorithm manipulates the visual properties of an image patch by aligning the shapes of curves. Its input contains an image X_0 , a specified reference generation curve denoted as c^* with the corresponding reference generation rates r_t^* , and a source image patch \mathcal{A} to be edited. We can define the marginalized generation curve over the image patch as:

$$c(X_0, \mathcal{A}) \triangleq \sum_{e_{ij} \in \mathcal{A}} c(X_0, e_{ij}) l(e_{ij}),$$

where $l(e_{ij})$ is a uniform distribution over the pixels in the patch \mathcal{A} . Our goal is to search for a desired image \bar{X}_0 whose marginalized generation curve matches that of c^* , formulated as:

$$\operatorname{argmin}_{\bar{X}_0} D(c(X_0, \mathcal{A}) | c^*), \quad (11)$$

where D is the distance metric. Since it is challenging to normalize the generation curve over the image patch, i.e. $c(X_t, \mathcal{A})$, we use the total variance (TV) distance as the metric D .

However, directly optimizing X_0 in the ambient space often leads to distortions due to the restricted nature of the data distribution. Accordingly, based on Eq. 4, we select its corresponding X_t as the optimization variable, which is situated in a diffused distribution and is thus more fault-tolerant. On the other hand, due to the computational burden, we conduct local optimization by sampling a pixel and a timestep per iteration. In summary, for each iteration, we sample a pixel e_{ij} and a time t_k based on the pixel distribution $l(e_{ij})$ and the generation rate distribution $c(X_0, \mathcal{A})$, respectively. The optimization objective is thus rewritten as:

$$\operatorname{argmin}_{X_t} E_{c(t_s | X_t, \mathcal{A}), l(e_{ij})} |c(t_s | X_t, e_{ij}) - c^*(t_s)|, \quad (12)$$

where $|\cdot|$ is the L_1 norm. We then optimize X_t by $X_t \leftarrow X_t - \eta \nabla_{X_t} |r_{t_s}(X_{t_s}, e_{ij}) - r_{t_s}^*|$ with η as the learning rate using the SGD optimizer. After the optimization, we recover \bar{X}_0 from the optimized X_t by Eq. 4. The optimization algorithm can be applied to a range of image manipulation tasks by specifying the reference generation curve and adding additional constraints in the objective function.

Localized Modification A typical requirement in applications is to edit only the image inside a given patch \mathcal{A} . However, our standard SGD scheme often modifies the entire image, which is undesirable. Simply applying a mask to X_t does not solve the problem either, because the mask is applied at the noised level, while the corresponding noiseless image \bar{X}_0 can still contain modifications outside \mathcal{A} . Instead, we propose to iteratively blend the noised original image, X_t , and the noised

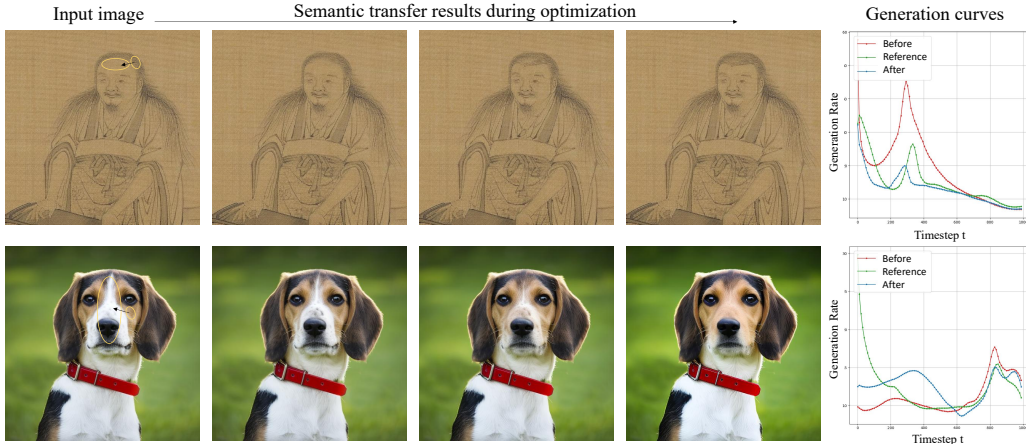


Figure 5: Semantic transfer results. Left: the input image and the transfer results during optimization. Right: generation curves before and after optimization, as well as the reference curve.

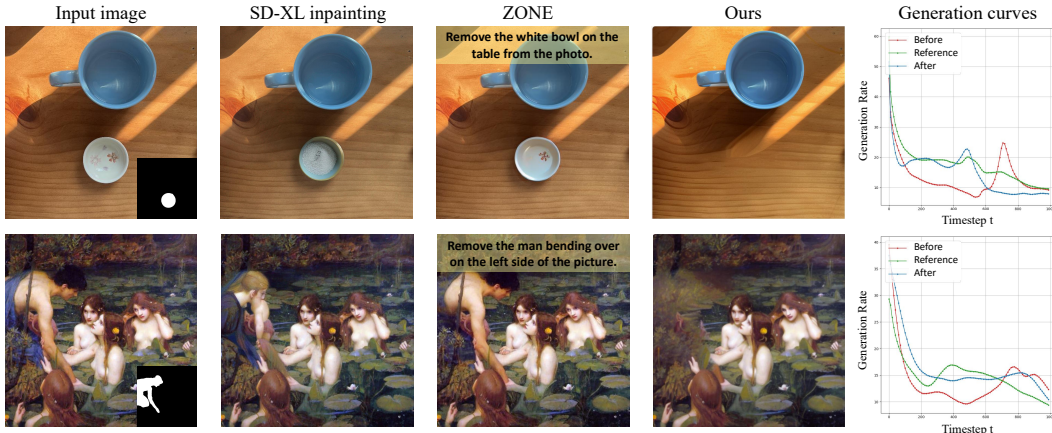


Figure 6: Object removal comparison. From left to right: the input image and object mask, the results of alternative approaches [26, 27] and ours, corresponding generation curves during optimization.

optimized image, \bar{X}_t , via $X_t \leftarrow \hat{X}_t \odot \mathcal{A} + X_t \odot \bar{\mathcal{A}}$, where $\bar{\mathcal{A}}$ is the complement of \mathcal{A} and \odot is the pixel-wise product. We perform such blending for $t > t_{\text{blend}}$ every 70 iterations. Here we only apply blending at a sufficiently high noise level ($t > t_{\text{blend}}$) so that the noiseless image has seamless patch boundaries around \mathcal{A} due to the nature of the reverse generation process.

5 Image Manipulation Applications

Many image manipulation tasks can be considered as the transformation of visual properties. This section demonstrates how our curve matching algorithm can flexibly perform various image manipulations using only a pre-trained unconditional diffusion model. Our generation curve provides a unified framework for many tasks and eliminates the need to train separate models for each of them or require large datasets for specific domains. For more results, please refer to our Appendix C.

5.1 Semantic Transfer

The semantic transfer task modifies a source region to match the semantic properties (e.g., color, material, texture) of a reference while maintaining other properties (e.g., depth, shape) unchanged. Due to the set of visual properties coupled within the curve, this problem can be inherently dealt with using our curve matching algorithm by specifying the reference curve of a pixel with desired

semantic properties. To avoid meaningless transfers from arbitrary references, we select the reference pixel from a region adjacent to the target area, limiting their difference within the expected properties.

Figure 5 illustrates our semantic transfer results as well as the generation rate curves before and after the optimization. In the second row, the goal is to turn the white fur on the dog’s face to a brown color. We select the reference pixel on its cheek, which has the desired brown color and is similar to the source area in terms of other aspects, e.g., both areas are fur on the dog. After optimization, the optimized curves align with the specified reference, and the white fur gradually turns brown.

5.2 Object Removal

Object removal involves replacing an object with the background it obscured, while keeping the rest of the image unchanged. Our curve matching algorithm addresses this by transferring the visual properties of the background to the pixels of the object to be removed. This process shares the same pipeline as semantic transfer, with the reference pixel selected from the expected background.

Method	$CLIP_{dir}\uparrow$	$CLIP_{sim}\downarrow$	$DINO_{sim}\downarrow$
ZONE [27]	0.2589	0.4824	0.433
SD-XL inpainting [26]	0.2617	0.4787	0.422
Ours	0.2629	0.4782	0.416

Table 1: Quantitative comparison of methods

Figure 6 compares the object removal results of our method and two recent approaches, i.e., SD-XL inpainting [26] and an instruction-based method, called ZONE [27]. The shortcomings of these two types of methods are primarily in the following aspects: Inpainting methods that are trained on masked images can be considered a form of re-sampling from the true image distribution conditioned on the unmasked region [28]. Although such re-sampling from high-density regions sometimes corresponds to the background, thereby achieving the goal of object removal, this approach is not stable. Occasionally, the object to be removed may be covered by another object. For instruction-based methods, they achieve image editing through a pre-trained model that accepts textual instructions. However, they sometimes fail to identify the objects described in the text instruction. In the case of removal, they often fail when dealing with complex occlusion scenarios.

We evaluate the performance on the test set from Emu Edit benchmark [29], where the input images, image captions before and after object removal, and the text instructions are provided. For the additional inputs required by our method, such as the mask and reference point, we use a segmentation tool and select the spatial locations. Since there is no exact metric for object removal tasks, we select three similarity-based metrics with CLIP [30] and DINO [24], i.e., $CLIP_{dir}$ for the similarity between the caption encoding difference and the image encoding difference before and after removal [29], $CLIP_{sim}$ and $DINO_{sim}$ for the similarity between the editing area before and after removal. The quantitative results reported in Table 1 validates the superior performance of our approach.

5.3 Saliency Manipulation

Saliency manipulation involves altering the saliency of an object while maintaining its identity. The high correlation between visual saliency and the fluctuation of the generation curve allows us to adjust saliency by modifying these fluctuations during curve optimization. Directly specifying a reference curve pattern with only a different fluctuation is challenging. However, we observe that, except for a brief period when t approaches 0, i.e., $t < t_b$, the salient curve is consistently higher and has distinct peaks compared to the non-salient curve, which maintains a lower and fixed value. Therefore, to increase (resp. decrease) saliency, we simply maximize (minimize) generation rates for $t > t_b$, with $t_b = 200$ in our implementation, where the reference curve is implicitly specified. We also use the feature alignment loss from UNet as described in [32] to preserve image content.

We present the saliency editing results in Figure 7, comparing our results and those of a recent approach RSG [31]. The results indicate that using curves as a measure and quantification of saliency is reasonable. By contrast, it is challenging for the existing methods to learn accurate visual saliency from the eye-tracking data. Consequently, they often focus on patterns such as color contrast and brightness, thus failing to produce harmonized results across diverse natural images.

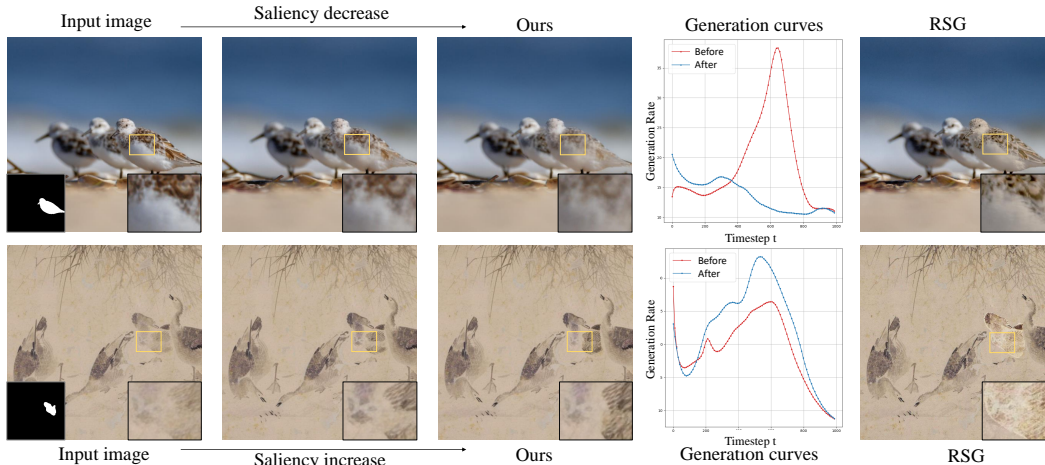


Figure 7: Saliency manipulation comparison. From left to right: input images and masks, intermediate and final results of ours, generation curves during optimization, results of an alternative approach [31].

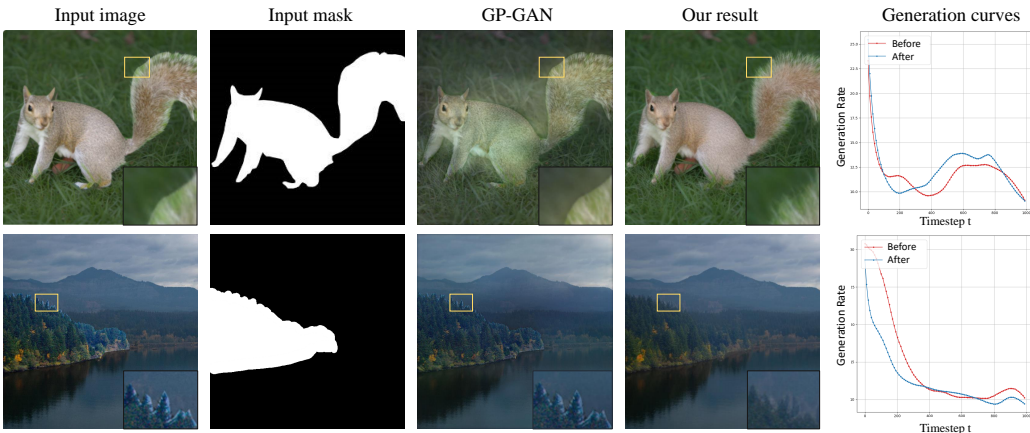


Figure 8: Image blending comparison. From left to right: input image, input mask, results of GP-GAN [33], our results, and the corresponding generation curves.

5.4 Image Blending

The Image blending task aims at blending a foreground image with a background image on boundaries. To accomplish this task, given a composite image, we define the boundary between the foreground and background as the salient region, since the boundaries contain undesirable and eye-catching seams. Therefore, we propose to reduce the visual saliency of the boundary region to make a natural transition. With our curve matching algorithm, we follow the same way as our saliency manipulation application, but minimize only the visual saliency at the boundary region of the foreground object.

In Figure 8, we show the results of our method and an existing approach [33]. In our experiments, we found that existing methods often perform well on specific types of images, and fail to produce universally satisfactory results across a variety of natural images. Instead, our approach consistently produces visually pleasing boundaries for the composite images.

6 Conclusion

In this work, we propose the generation rate, which corresponds to the geometric deformation of the manifold over time around a image component. Through comprehensive analytical evaluations, we show that the time-varying geometric deformation exhibits a high correlation with visual saliency of

the image component. In addition, manipulating the generation curves with different loss functions provides a unified framework for a row of image manipulation tasks. Future research could explore more applications and address the limitations of our generation curve. For instance, our curve optimization algorithm requires first-order differentiation computation and thus requires approximately 10 minutes for 300 iterations including the pre-processing, running on a single Nvidia 4090 GPU with 24GB memory. On the other hand, for image manipulation tasks, since different objects have varying visual appearances and thus different generation curves, it causes varying convergence speeds and thus different numbers of iterations during curve optimization.

References

- [1] Diederik P. Kingma and Max Welling. Auto-Encoding Variational Bayes. In *2nd International Conference on Learning Representations, ICLR 2014*, 2014.
- [2] Ian Goodfellow, Jean Pouget-Abadie, Mehdi Mirza, Bing Xu, David Warde-Farley, Sherjil Ozair, Aaron Courville, and Yoshua Bengio. Generative adversarial nets. *Advances in neural information processing systems*, 27, 2014.
- [3] Georgios Arvanitidis, Lars Kai Hansen, and Søren Hauberg. Latent space oddity: on the curvature of deep generative models. In *6th International Conference on Learning Representations, ICLR 2018*. OpenReview.net, 2018.
- [4] Hang Shao, Abhishek Kumar, and P. Thomas Fletcher. The riemannian geometry of deep generative models. *2018 IEEE/CVF Conference on Computer Vision and Pattern Recognition Workshops (CVPRW)*, pages 428–4288, 2017.
- [5] Jascha Sohl-Dickstein, Eric Weiss, Niru Maheswaranathan, and Surya Ganguli. Deep unsupervised learning using nonequilibrium thermodynamics. In *International conference on machine learning*, pages 2256–2265. PMLR, 2015.
- [6] Jonathan Ho, Ajay Jain, and Pieter Abbeel. Denoising diffusion probabilistic models. *Advances in neural information processing systems*, 33:6840–6851, 2020.
- [7] Yang Song, Jascha Sohl-Dickstein, Diederik P Kingma, Abhishek Kumar, Stefano Ermon, and Ben Poole. Score-based generative modeling through stochastic differential equations. In *International Conference on Learning Representations*, 2021.
- [8] Jiaming Song, Chenlin Meng, and Stefano Ermon. Denoising diffusion implicit models. In *9th International Conference on Learning Representations, ICLR 2021*, 2021.
- [9] Joshua B. Tenenbaum, Vin de Silva, and John C. Langford. A global geometric framework for nonlinear dimensionality reduction. *Science*, 290 5500:2319–23, 2000.
- [10] Sam T. Roweis and Lawrence K. Saul. Nonlinear dimensionality reduction by locally linear embedding. *Science*, 290 5500:2323–6, 2000.
- [11] Nutan Chen, Alexej Klushyn, Richard Kurle, Xueyan Jiang, Justin Bayer, and Patrick Smagt. Metrics for deep generative models. In *International Conference on Artificial Intelligence and Statistics*, pages 1540–1550. PMLR, 2018.
- [12] Salah Rifai, Pascal Vincent, Xavier Muller, Xavier Glorot, and Yoshua Bengio. Contractive auto-encoders: Explicit invariance during feature extraction. In *Proceedings of the 28th international conference on international conference on machine learning*, pages 833–840, 2011.
- [13] Salah Rifai, Yann N Dauphin, Pascal Vincent, Yoshua Bengio, and Xavier Muller. The manifold tangent classifier. In J. Shawe-Taylor, R. Zemel, P. Bartlett, F. Pereira, and K.Q. Weinberger, editors, *Advances in Neural Information Processing Systems*, volume 24. Curran Associates, Inc., 2011.
- [14] Abhishek Kumar, Prasanna Sattigeri, and Tom Fletcher. Semi-supervised learning with gans: Manifold invariance with improved inference. *Advances in neural information processing systems*, 30, 2017.
- [15] Yoshua Bengio, Aaron Courville, and Pascal Vincent. Representation learning: A review and new perspectives. *IEEE transactions on pattern analysis and machine intelligence*, 35(8):1798–1828, 2013.
- [16] Aditya Ramesh, Youngduck Choi, and Yann LeCun. A spectral regularizer for unsupervised disentanglement, 2019.

- [17] Andrey Voynov and Artem Babenko. Unsupervised discovery of interpretable directions in the gan latent space. In *International Conference on Machine Learning*, 2020.
- [18] Mingi Kwon, Jaeseok Jeong, and Youngjung Uh. Diffusion models already have a semantic latent space. In *International Conference on Learning Representations, ICLR*, 2023.
- [19] Yong-Hyun Park, Mingi Kwon, Jaewoong Choi, Junghyo Jo, and Youngjung Uh. Understanding the latent space of diffusion models through the lens of riemannian geometry. *Advances in Neural Information Processing Systems*, 36:24129–24142, 2023.
- [20] René Haas, Inbar Huberman-Spiegelglas, Rotem Mulayoff, and Tomer Michaeli. Discovering interpretable directions in the semantic latent space of diffusion models. *ArXiv*, abs/2303.11073, 2023.
- [21] Robin Rombach, Andreas Blattmann, Dominik Lorenz, Patrick Esser, and Björn Ommer. High-resolution image synthesis with latent diffusion models. In *Proceedings of the IEEE/CVF conference on computer vision and pattern recognition*, pages 10684–10695, 2022.
- [22] Ali Borji and Laurent Itti. Cat2000: A large scale fixation dataset for boosting saliency research. *CVPR 2015 workshop on "Future of Datasets"*, 2015. arXiv preprint arXiv:1505.03581.
- [23] Richard Zhang, Phillip Isola, Alexei A. Efros, Eli Shechtman, and Oliver Wang. The unreasonable effectiveness of deep features as a perceptual metric. In *2018 IEEE Conference on Computer Vision and Pattern Recognition, CVPR 2018*, pages 586–595. Computer Vision Foundation / IEEE Computer Society, 2018.
- [24] Mathilde Caron, Hugo Touvron, Ishan Misra, Hervé Jégou, Julien Mairal, Piotr Bojanowski, and Armand Joulin. Emerging properties in self-supervised vision transformers. In *Proceedings of the IEEE/CVF international conference on computer vision*, pages 9650–9660, 2021.
- [25] Jooyoung Choi, Jungbeom Lee, Chaehun Shin, Sungwon Kim, Hyunwoo Kim, and Sungroh Yoon. Perception prioritized training of diffusion models. In *IEEE/CVF Conference on Computer Vision and Pattern Recognition, CVPR 2022*, pages 11462–11471. IEEE, 2022.
- [26] Dustin Podell, Zion English, Kyle Lacey, Andreas Blattmann, Tim Dockhorn, Jonas Müller, Joe Penna, and Robin Rombach. Sdxl: Improving latent diffusion models for high-resolution image synthesis, 2023.
- [27] Shanglin Li, Bohan Zeng, Yutang Feng, Sicheng Gao, Xuhui Liu, Jiaming Liu, Li Lin, Xu Tang, Yao Hu, Jianzhuang Liu, et al. Zone: Zero-shot instruction-guided local editing. *arXiv preprint arXiv:2312.16794*, 2023.
- [28] Litu Rout, Advait Parulekar, Constantine Caramanis, and Sanjay Shakkottai. A theoretical justification for image inpainting using denoising diffusion probabilistic models, 2023.
- [29] Shelly Sheynin, Adam Polyak, Uriel Singer, Yuval Kirstain, Amit Zohar, Oron Ashual, Devi Parikh, and Yaniv Taigman. Emu edit: Precise image editing via recognition and generation tasks. *arXiv preprint arXiv:2311.10089*, 2023.
- [30] Alec Radford, Jong Wook Kim, Chris Hallacy, Aditya Ramesh, Gabriel Goh, Sandhini Agarwal, Girish Sastry, Amanda Askell, Pamela Mishkin, Jack Clark, et al. Learning transferable visual models from natural language supervision. In *International conference on machine learning*, pages 8748–8763. PMLR, 2021.
- [31] S Mahdi H Miangoleh, Zoya Bylinskii, Eric Kee, Eli Shechtman, and Yağiz Aksoy. Realistic saliency guided image enhancement. In *Proceedings of the IEEE/CVF Conference on Computer Vision and Pattern Recognition*, pages 186–194, 2023.
- [32] Chong Mou, Xintao Wang, Jiechong Song, Ying Shan, and Jian Zhang. Dragondiffusion: Enabling drag-style manipulation on diffusion models, 2023.
- [33] Huikai Wu, Shuai Zheng, Junge Zhang, and Kaiqi Huang. Gp-gan: Towards realistic high-resolution image blending. In *Proceedings of the 27th ACM international conference on multimedia*, pages 2487–2495, 2019.
- [34] Antonio Criminisi, Patrick Pérez, and Kentaro Toyama. Region filling and object removal by exemplar-based image inpainting. *IEEE Transactions on Image Processing*, 13:1200–1212, 2004.

- [35] Roman Suvorov, Elizaveta Logacheva, Anton Mashikhin, Anastasia Remizova, Arsenii Ashukha, Aleksei Silvestrov, Naejin Kong, Harshith Goka, Kiwoong Park, and Victor Lempitsky. Resolution-robust large mask inpainting with fourier convolutions. In *Proceedings of the IEEE/CVF winter conference on applications of computer vision*, pages 2149–2159, 2022.
- [36] Andreas Lugmayr, Martin Danelljan, Andres Romero, Fisher Yu, Radu Timofte, and Luc Van Gool. Repaint: Inpainting using denoising diffusion probabilistic models. In *Proceedings of the IEEE/CVF conference on computer vision and pattern recognition*, pages 11461–11471, 2022.
- [37] Tim Brooks, Aleksander Holynski, and Alexei A Efros. Instructpix2pix: Learning to follow image editing instructions. In *Proceedings of the IEEE/CVF Conference on Computer Vision and Pattern Recognition*, pages 18392–18402, 2023.
- [38] Xingang Pan, Ayush Tewari, Thomas Leimkühler, Lingjie Liu, Abhimitra Meka, and Christian Theobalt. Drag your gan: Interactive point-based manipulation on the generative image manifold. In *ACM SIGGRAPH 2023 Conference Proceedings*, pages 1–11, 2023.
- [39] Amir Hertz, Ron Mokady, Jay Tenenbaum, Kfir Aberman, Yael Pritch, and Daniel Cohen-Or. Prompt-to-prompt image editing with cross-attention control. In *The Eleventh International Conference on Learning Representations, ICLR 2023*, 2023.
- [40] Kfir Aberman, Ju He, Yossi Gandelsman, Inbar Mosseri, David E. Jacobs, Kai Kohlhoff, Yael Pritch, and Michael Rubinstein. Deep saliency prior for reducing visual distraction. *2022 IEEE/CVF Conference on Computer Vision and Pattern Recognition (CVPR)*, pages 19819–19828, 2021.
- [41] Youssef A. Mejjati, Celso F. Gomez, Kwang In Kim, Eli Shechtman, and Zoya Bylinskii. Look here! a parametric learning based approach to redirect visual attention. *ArXiv*, abs/2008.05413, 2020.
- [42] Lai Jiang, Mai Xu, Xiaofei Wang, and Leonid Sigal. Saliency-guided image translation. *2021 IEEE/CVF Conference on Computer Vision and Pattern Recognition (CVPR)*, pages 16504–16513, 2021.
- [43] Patrick Pérez, Michel Gangnet, and Andrew Blake. Poisson image editing. *ACM SIGGRAPH 2003 Papers*, 2003.
- [44] Lingzhi Zhang, Tarmily Wen, and Jianbo Shi. Deep image blending. In *Proceedings of the IEEE/CVF winter conference on applications of computer vision*, pages 231–240, 2020.
- [45] He Zhang, Jianming Zhang, Federico Perazzi, Zhe Lin, and Vishal M Patel. Deep image compositing. In *Proceedings of the IEEE/CVF winter conference on applications of computer vision*, pages 365–374, 2021.
- [46] Yazhou Xing, Yu Li, Xintao Wang, Ye Zhu, and Qifeng Chen. Composite photograph harmonization with complete background cues. *Proceedings of the 30th ACM International Conference on Multimedia*, 2022.
- [47] Li Niu, Wenyan Cong, Liu Liu, Yan Hong, Bo Zhang, Jing Liang, and Liqing Zhang. Making images real again: A comprehensive survey on deep image composition, 2024.
- [48] Wenyan Cong, Jianfu Zhang, Li Niu, Liu Liu, Zhixin Ling, Weiyuan Li, and Liqing Zhang. Dovenet: Deep image harmonization via domain verification. In *CVPR*, 2020.

A Curve Matching Algorithm

As described in Section 4, our curve matching algorithm manipulates the original image X_0 to align the generation curves of a source area \mathcal{A} and a reference pixel p^* . When applied for different image manipulation tasks, we flexibly select the reference pixel and modify the loss function \mathcal{L} to achieve different goals. The default hyperparameter setting is $t = 700$ and learning rate $\eta = 0.02$. The iteration number ranges from 30 to 300 for different tasks, as we show their intermediate results during the optimization process. We use the pre-trained unconditional diffusion model, stable-diffusion-2-1-base, for all our experiments.

We present the details in Algorithm 1. The basic idea is to update X_t , transformed from the input X_0 , in order to align the generation curves of the source area $c(X_t, \mathcal{A})$ and the curve $c^* = c(X_t, p^*)$ of the reference pixel p^* for each channel. Specifically, we first transform X_0 to X_t via the deterministic process, and pre-compute the generation curve of the reference pixel and that of a random pixel within the source area, i.e. $c^* = r_t(X_t, v^*)$, $c_a = r_t(X_t, v_a)$. Here we use the curve of a random point in \mathcal{A} to represent the $c(X_t, \mathcal{A})$. Then we start the iterative optimization. In each iteration, we sample a pixel p_k within the source area randomly and a time t_k based on the cumulative distribution of c_a , the generation curve of the representative source pixel. The optimization variable X_t is transformed to X_{t_k} , which is used to compute the generation rate $r_{t_k}(X_{t_k}, v_k)$ and the loss function $\mathcal{L} = |r_{t_k}(X_{t_k}, v_k) - r_{t_k}^*|$. Then we update X_t with an Adam optimizer. After finishing the optimization, e.g. reaching the maximum iteration number, we recover X_t back to \tilde{X}_0 via Eq. 4.

Curve updating. The optimization objective requires to sample t_k according to the curve of the source area, which in turn varies during the optimization and is time-consuming to compute. Firstly, to simplify the computation, we sample a representative pixel p_a within the source area and compute its generation curve, i.e. c_a , to represent the curve of the source area. On the other hand, we update the curve after every $m = 50$ iteration steps. Additionally, when the reference curve also varies, e.g. when the reference pixel lies within the source area, we update the reference curve as well.

Algorithm 1 Curve Matching Algorithm

Input: Image X_0 , source pixel set \mathcal{A} , reference pixel p^* , hyperparameter t , iteration number N

```
/* Initialization */
1: Transform  $X_0$  through Eq. 4 to obtain  $X_t$  // Initialize the optimization variable
2: Initialize directional vector  $v^*$  for  $p^*$  and  $v_a$  for a randomly sampled source pixel  $p_a \in \mathcal{A}$ 

/* Pre-processing */
3:  $c_a \leftarrow r_t(X_t, v_a)$ ,  $c^* \leftarrow r_t(X_t, v^*)$  // Compute curves  $c_a$  and  $c_r$  for  $p_a$  and  $p_r$  respectively

/* Curve optimization with  $X_t$  as the variable */
4: for  $k = 1$  to  $N$  do
5:   Sample a random source pixel  $p_k \in \mathcal{A}$  and initialize its corresponding vector  $v_k$ 
6:   Sample a time  $t_k$  based on the normalized  $c_a$ 
7:   Transform  $X_t$  to  $X_{t_k}$  through Eq. 4 without gradients
8:   Compute generation rate  $r_{t_k}(X_{t_k}, v_k)$ 
9:   Compute the loss  $\mathcal{L} = |r_{t_k}(X_{t_k}, v_k) - c^*(t_k)|$ 
10:  Update  $X_t \leftarrow X_t - \eta \nabla \mathcal{L}$ 
11: end for

/* Generate the manipulated image from optimized  $X_t$  */
12: Transform the edited  $X_t$  to  $\tilde{X}_0$  through Eq. 4
```

B Visual Analysis Experiments

In the following visual analysis experiments, we take the 0-th channel to represent a pixel for acceleration purpose. Although the generation curves of the channels at the same pixel have different values, we empirically found that they exhibit the same trend, allowing us to take one channel as the representative.

B.1 Visual Saliency Experiment

Experiment setting. We validate the connection between the fluctuation of our generation curve and the visual saliency of images, as described in Section 3.3. The experiment is conducted on the MIT saliency benchmark CAT2000 [22], which provides the collected eye-tracking data of images from human observers and the pre-processed saliency map. For each image, we randomly select one pixel within maximum saliency values and one within minimum values as the salient pixel and non-salient pixel. For the generation curves at the two pixels, we compute its local variance for $t > 200$ (to ignore the abrupt rise when t is close to 0) over a sliding window of length $k = 5$ and take their average to represent the curve fluctuation.

Discussion. Figure 9 presents the example images and the generation curves corresponding to the selected pixels. For the example on the left, the salient pixel corresponds to the blue curve with obviously higher fluctuation than the red curve. In our experiment, we found that our estimated curve fluctuation often reflects the visual saliency well for natural images. However, for some special cases, the noise inherent in eye-tracking data causes the inaccurate spatial location of the salient and non-salient pixels, and thus significantly interfering with our pixel-level calculations. For the line drawing images on the right, our curve fluctuation is not consistent with the ground-truth visual saliency. The red pixel is marked as non-salient pixel, while it corresponds to a higher curve fluctuation since it is located in the region with dense line drawings.

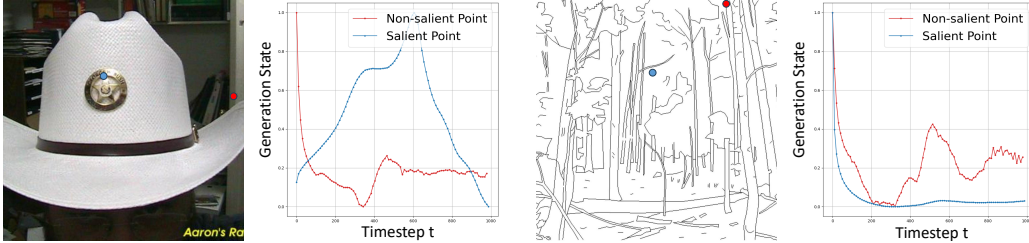


Figure 9: The salient pixel (blue) and non-salient pixel (red) on the images and their corresponding generation curves. The left shows that our curve fluctuation is often consistent with the ground-truth saliency for natural images. The right is an inconsistent case with the special line drawing images.

B.2 Two types of Generation Curves

Experiment setting. Given an image and the mask of a small object, we compare our generation curve and another alternative approach, both of which estimate the generation rates of the small object at different timesteps. The alternative approach computes a perceptual-based curve that utilizes perceptual loss to estimate the generation rates of a local region. The experiments are as follows.

- **Perceptual-based curve.** For each timestep during the diffusion process, given the noised image X_t , we can predict the \hat{X}_0 with DDIM (Eq 4) and decode the corresponding RGB image \hat{I} . Then we use the pre-trained DINO model [24] to compute the perceptual loss between the predicted \hat{I} and the original image I w.r.t. the region of the specified small object. The perceptual loss is defined as the cosine distance between the features $DINO(\hat{I} \odot M)$ and $DINO(I \odot M)$, corresponding to the generation state at timestep t that ranges from 0 to 1. And its derivatives can be considered as an approximation of the generation rates.
- **Our generation curve.** Due to the compressive nature of LDM and the sensitivity of our method at the pixel-channel level, we select the central pixel of the specified small object as the representative spatial location to compute our generation curve. That is, given the noised image X_t , we construct the vector v based on the pixel location and compute the generation rates $r_t(X_t, v)$ with Eq 10 to obtain the generation curve.

Discussion. Figure 10 presents the curves of two example images, both ours and the perceptual-based curves. Note that we normalize the curves into the range $[0, 1]$ for a better visualization. As described in Section 3.3, the two types of curves exhibit similar trends, especially with their main peaks occurring at close timesteps. It validates that both the two curves reflect the generation rates. On the other hand, compared to the intuitive perceptual-based curves, our generation curve is more applicable

to many potential tasks. Firstly, the perceptual loss is object-wise rather than pixel-wise. It prevents its analysis and application to more fine-grained generation patterns. Secondly, the perceptual loss can only distinguish the prominent foreground features. Consequently, the perceptual-based curve often exhibits heavy noise or even negative values with less prominent visual features, especially the flat background, as shown in Figure 11.

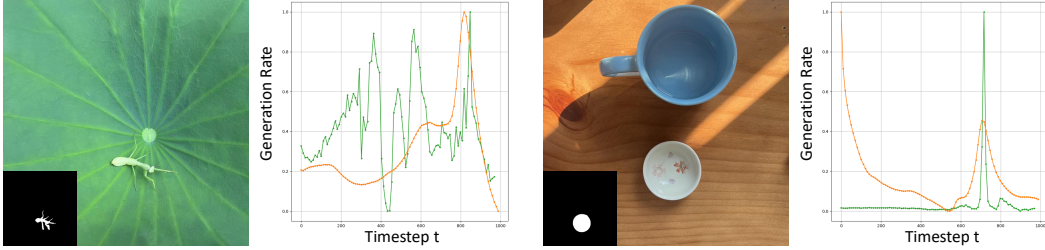


Figure 10: Two types of generation curves for the masked small object in the image. Green: the perceptual-based curve; Orange: our generation curve. All the curves are normalized into range $[0, 1]$.

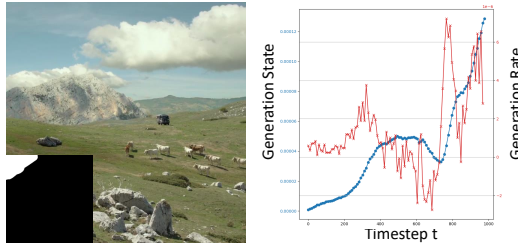


Figure 11: We plot the generation state (blue) and generation rate (red) estimated by the perceptual-based loss. For background areas without prominent visual features, the perceptual-based curves (red) tend to exhibit heavy noise or even negative generation rates.

C Application Details

C.1 Semantic Transfer

The semantic transfer application shares the same pipeline with our object removal application, except that we select a representative pixel of a surrounding object as the reference. We demonstrate more visual results in Figure 12. It enables interactive editing with only a click on the image to specify the reference. However, since the generation curves involve various visual properties, sometimes the transfer results don't exhibit the desired visual effects. For example, as shown in Figure 13, it transfers the material but not the color in the two examples.

C.2 Object Removal

Experiment setting. We conduct the comparison experiment on the test set from Emu Edit benchmark [29]. For the object removal task, it provides the original images, the input and output captions, and the text instructions to specify the objects to be removed. We pre-process the test set with an image segmentation tool to obtain the masks of the objects to be removed. The quantitative evaluation is performed on a random subset of 100 images from this test set. Note that there's no need for the training set since we utilize the pre-trained models in all our experiments.

The related works often utilize image inpainting [34, 35, 36, 26] or instruction-based image editing [37, 38, 39] for the object removal task. The former resamples the editing area, which is then likely to fall into the high-density distributions, i.e. image background. The latter fine-tunes the pre-trained image generation model to take the text instructions as conditions. We compare with the SD-XL inpainting [26] and instruction-based method ZONE [27] in our experiments:

- **SD-XL inpainting.** We input the original image and the object mask to the SD-XL model, i.e. stable-diffusion-xl-1.0-inpainting-0.1, and obtain the inpainted image as the result.

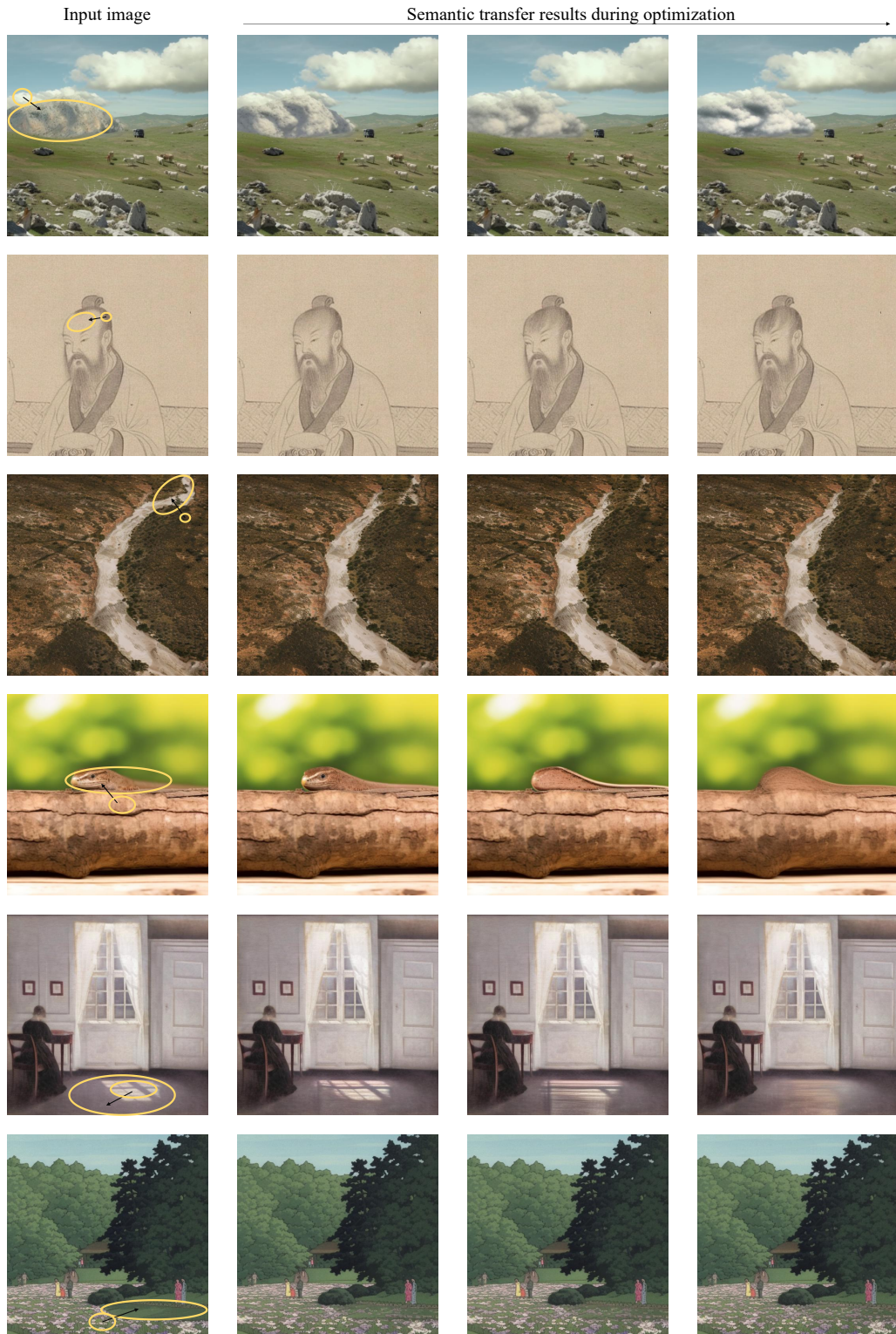


Figure 12: More results of semantic transfer. The left column shows the input image, where the arrows indicate the semantic transfer from the reference to source area. From left to right, we show the intermediate results during the optimization.



Figure 13: Failure cases of semantic transfer. The material and depth features are transferred but not the color.

- **ZONE.** We take the original image and the text instruction as input and the generated image as result. Note that the pre-processed object mask is used in the composition of the generated image for a precise local editing.
- **Ours.** The input includes the original image, the object mask as the source area, a selected surrounding background pixel as the reference. Note that the tedious selection of reference pixels can be omitted for simple cases with a uniform background, as described in the following implementation.

Implementation. To alleviate the manual selection of reference pixels, we adopt an approximation solution for the simple cases. That is, we divide the test set into two types: one containing the target objects located on uniform backgrounds, and the other with complex and varying backgrounds. For the former, instead of using the generation curve at a manually selected reference pixel, we define a fixed pseudo curve to replace it. Specifically, since the generation curves at background locations often follow the common pattern with stable and lower values, we directly minimize the generation rate values at the target area for $t > 200$, i.e. $\mathcal{L} = |r(X_{t_i}, p_i)|$. For the latter, we manually select the reference pixels and invoke our curve matching algorithm as described in Algorithm 1. We experimentally found that the pseudo curve solution is enough for most images (more than 80 out of the 100 images in our quantitative evaluation, Table 1 in the main paper).

Results and failure cases. We present more results of object removal in Figure 14. Our approach outperforms the alternatives in terms of generating clean and reasonable results. However, we also notice some failure cases when the background is complex. As shown in Figure 15, sometimes it may be hard to specify a reference pixel representative for the background. This often causes distorted results at the region of the object to be removed.

C.3 Saliency Manipulation

Experiment setting. Saliency manipulation refers to increase or decrease the saliency of a specific object as one expects, while maintaining the image content as unchanged as possible [40, 41, 42, 31]. The input contains the original image and a mask indicating the region to be edited. In our experiments, we compare against a recent saliency-based image manipulation approach [31]. This approach, denoted as RSG, optimizes the image with a saliency loss using a pre-trained saliency model and a realism loss to prevent frequent unrealistic edits. We use their released code and the parameters in our experiments. As for our approach, we eliminate the reference curve, but directly minimize or maximize the generation rate values for $t > 200$ at the editing region to control the saliency. At the same time, we define a feature alignment loss to preserve the original image content. The feature alignment loss is defined as the difference between the U-Net intermediate feature maps before and after the editing. In summary, we replace the loss in Algorithm 1 as $\mathcal{L} = \lambda_1 |r_{t_k}(X_{t_k}, p_k)|^{\lambda_2} + \sum_i |U_i(X_{t_k}) - U_i(X_t)|$, where $\lambda_1 = 50$ is a weighting parameter and λ_2 takes values 1 or -1 to decrease or increase the saliency, respectively. And U_i represents the U-Net layers which outputs the intermediate feature maps. We set the iteration number $N = 70$ for the saliency manipulation task.

Results and failure cases. We present the saliency increase and decrease examples in Figure 16 and 17. As the iteration number increases during the optimization, our approach obtains edited objects with saliency varies as expected. Increasing the saliency results in sharp color contrast and more visual details, while decreasing the saliency results in faded visual effects. We also present the failure cases in Figure 18. It is worth noting that all the saliency manipulation approaches require a

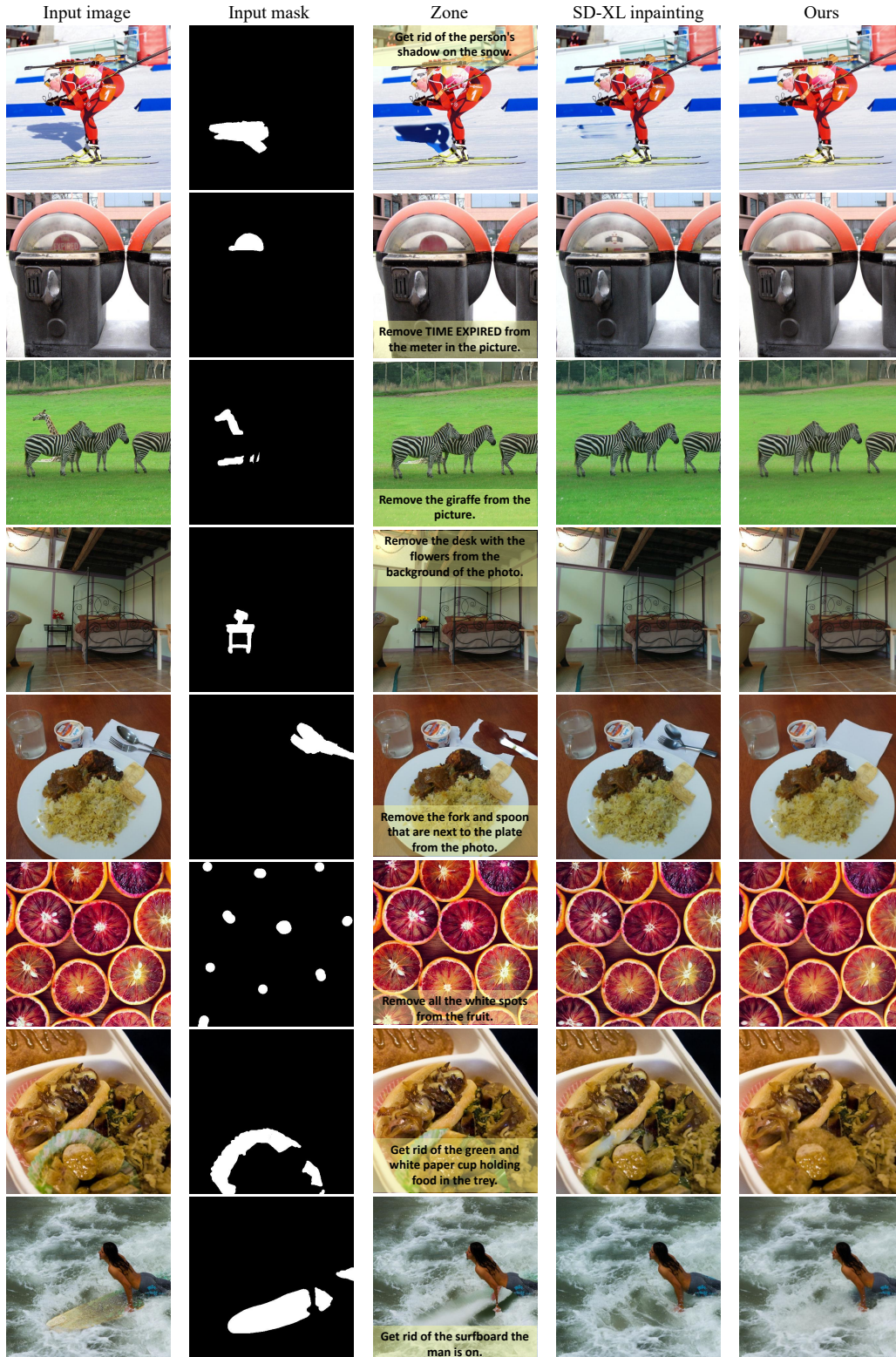


Figure 14: More object removal results. From left to right: the input image and the input object mask, the results of the instruction-based method ZONE [27], SD-XL inpainting [26], and our approach.



Figure 15: Failure cases of object removal application.

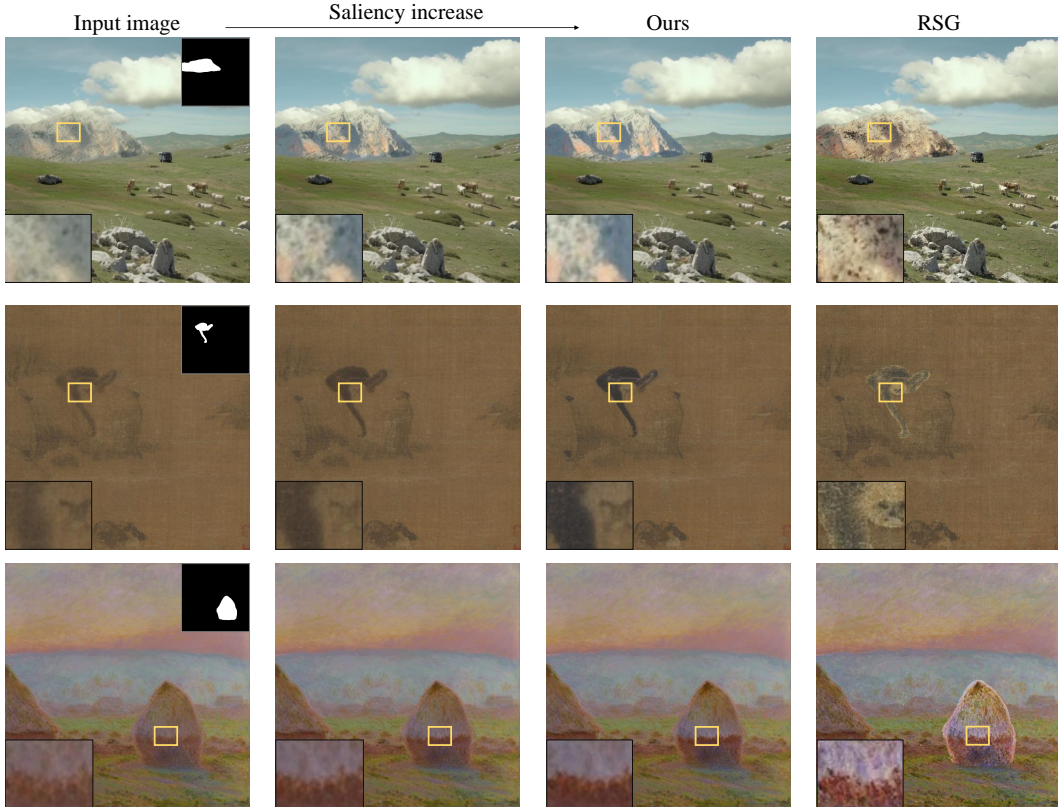


Figure 16: Saliency increasing results. From left to right: the input image, the intermediate and final results of our approach, the result of RSG [31].

balance between local editing and the preservation of image content. Sometimes, forcing the saliency variation may cause the altering of the original identity and object distortion.

C.4 Image Blending

Experiment setting. Image blending aims to create a natural boundary transition for the compositional images [43, 33, 44, 45, 46, 47]. We evaluate the image blending results on the iHarmony4 dataset [48]. It provides the synthesized composite image with inconsistent foreground and background, as well as the corresponding foreground masks. To conduct the experiment with our approach, we apply the erosion filter with kernel size $k = 3$ on the given mask and take the eroded region as the source area of our curve matching algorithm. We use the algorithm with loss $\mathcal{L} = \lambda_1 |r_{t_k}(X_{t_k}, p_k)| + \sum_i |U_i(X_{t_k}) - U_i(X_t)|$ to complete this task, where $\lambda_1 = 50$ is a weighting parameter and p_i are the pixels within the eroded region of the mask. We set the iteration number $N = 100$ for the image blending task.

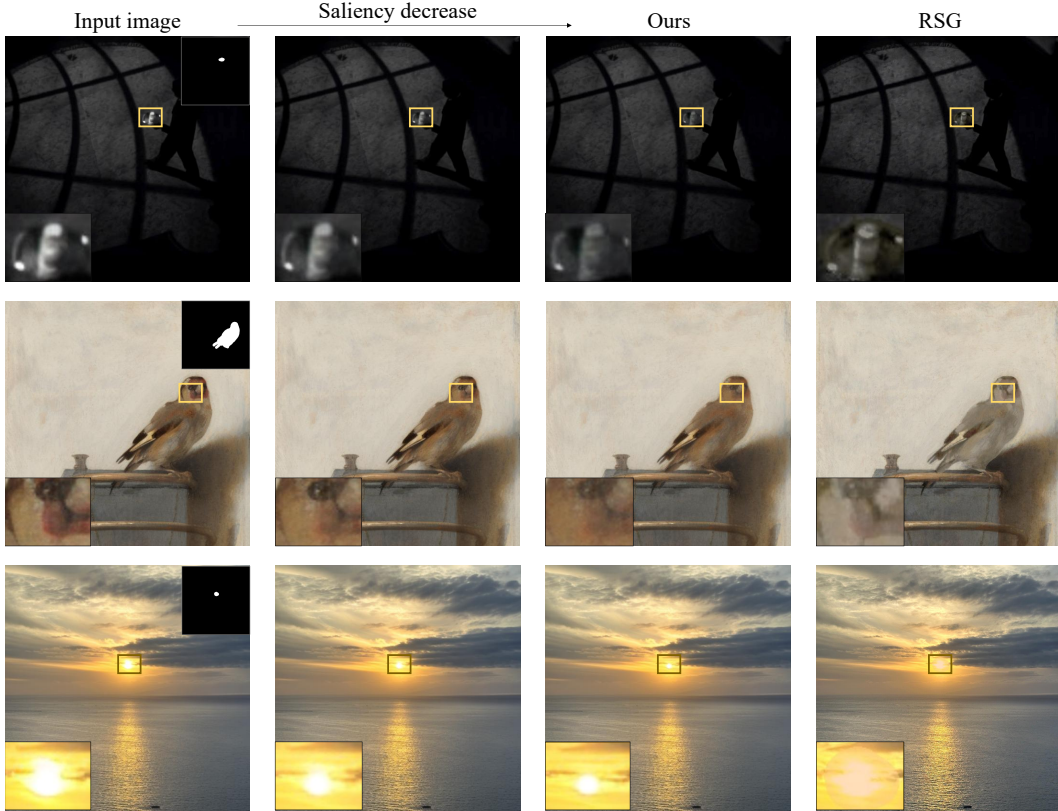


Figure 17: Saliency decreasing results. From left to right: the input image, the intermediate and final results of our approach, the result of RSG [31].

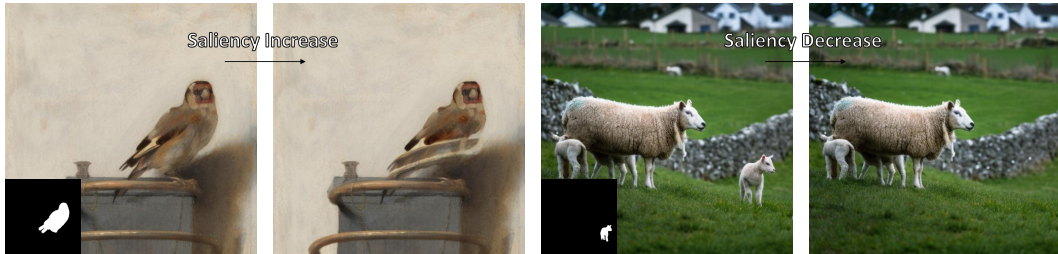


Figure 18: Failure cases of saliency manipulation.

Results and failure cases. When compared to [33] in Figure 8, this approach requires both the complete background and foreground images as input, Therefore, we utilize online tools that combines the inpainting [35] and post-processing techniques to provide a suitable background, as shown in Figure 19. We present more results in Figure 20. Our approach is able to produce a natural and smooth transition at the boundary. However, the smooth transition often corresponds to blurred details. As a consequence, the image details might be smoothed out during the blending, such as the beak of the bird and the leaves on the tree in Figure 21.

D Broader Impact

Similar to other image manipulation technologies, our generation curve matching algorithm also suffer the potential ethical implications such as disinformation or generating fake images. We recognize the potential ethical concerns that could emerge from utilizing our approach. We strongly encourage the creation and application of social and technical safeguards to mitigate potential misuse,

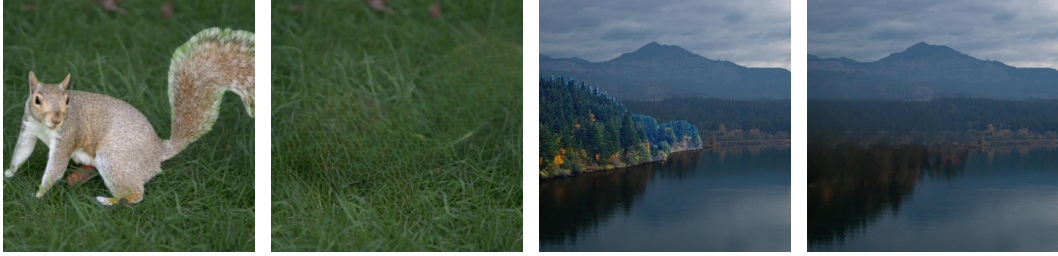


Figure 19: Provided background for GP-GAN [33] in image blending.

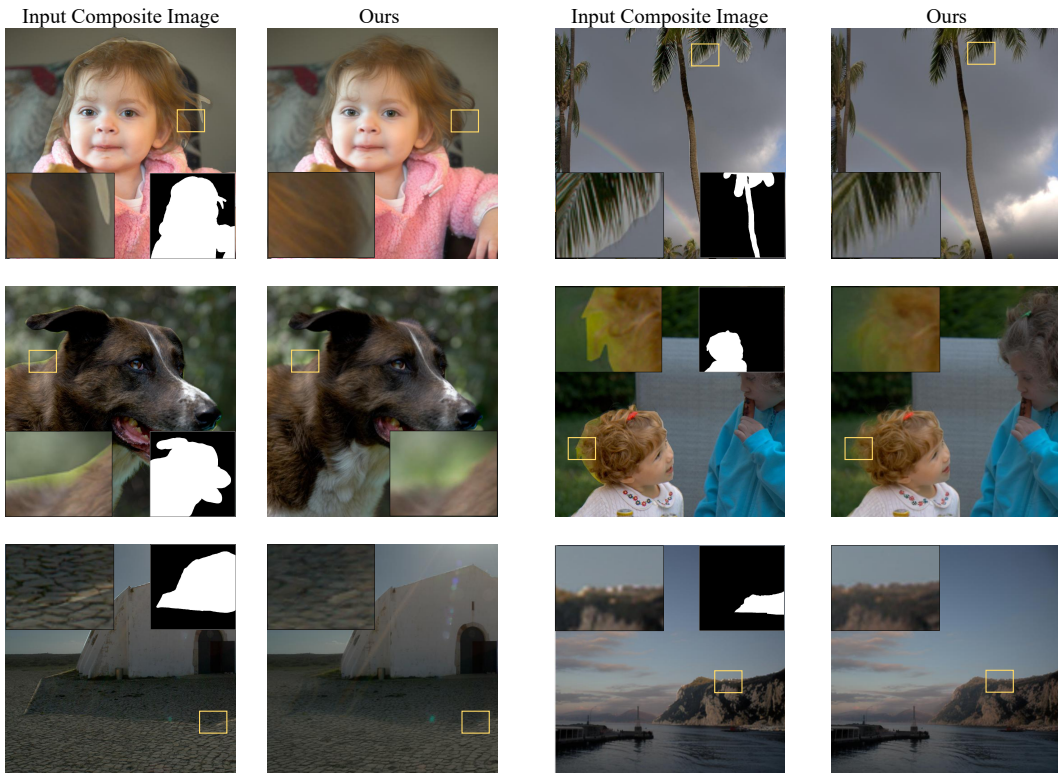


Figure 20: Image blending results. For each example, we show the input composite image and the foreground mask, as well as the result of our approach.



Figure 21: Failure cases of image blending. Although we achieve a natural blending at the boundary, it loses the small details such as the beak of the bird and the leaves on the tree.

such as the dissemination of disinformation or propaganda. We are dedicated to upholding fairness and non-discrimination, legal adherence, and research integrity in our endeavors.